INTERNATIONAL JOURNAL OF CLIMATOLOGY
Int. J. Climatol. (2015)
Published online in Wiley Online Library
(wileyonlinelibrary.com) DOI: 10.1002/joc.4428

RMetS
Royal Meteorological Society

Analysis of oceans' influence on spring time rainfall variability over Southeastern South America during the 20th century

Verónica Martín-Gómez* and Marcelo Barreiro

Instituto de Física, Facultad de Ciencias, Universidad de la República, Montevideo, Uruguay

ABSTRACT: Southeastern South America (SESA) rainfall is influenced by the tropical Pacific, Atlantic and Indian Oceans. At the same time, these tropical oceans interact with each other inducing sea surface temperature anomalies in remote basins through atmospheric and oceanic teleconnections.

In this study, we employ a tool from complex networks to analyse the collective influence of the three tropical oceans on austral spring rainfall variability over SESA during the 20th century. To do so we construct a climate network considering as nodes the observed Niño3.4, Tropical North Atlantic (TNA), and Indian Ocean Dipole (IOD) indices, together with an observed and simulated precipitation (PCP) index over SESA. The mean network distance is considered as a measure of synchronization among all these phenomena during the 20th century.

The approach allowed to uncover two main synchronization periods characterized by different interactions among the oceanic and precipitation nodes. Whereas in the 1930s El Niño and the TNA were the main tropical oceanic phenomena that influenced SESA precipitation variability, during the 1970s they were El Niño and the IOD. The influence of El Niño on SESA precipitation variability might be understood through an increase of the northerly transport of moisture in lower-levels and advection of cyclonic vorticity in upper-levels. On the other hand, the interaction between the IOD and PCP can be interpreted in two possible ways. One possibility is that both nodes (IOD and PCP) are forced by El Niño. Another possibility is that the Indian Ocean warming influences rainfall over SESA through the eastward propagation of Rossby waves as suggested previously. Finally, the influence of TNA on SESA precipitation persists even when the El Niño signal is removed, suggesting that SST anomalies in the TNA can directly influence SESA precipitation and further studies are needed to elucidate this connection.

KEY WORDS synchronization events; climate variability; tropical ocean teleconnections; tropic-extratropic teleconnections; precipitation over SESA

Received 25 April 2014; Revised 8 May 2015; Accepted 1 June 2015

1. Introduction

Rainfall in Southeastern South America (SESA) presents large variability from interannual to multidecadal time scales that has significant agricultural, environmental and economic impacts (e.g. Baethgen and Magrin, 2000; Podesta *et al.*, 2002; Hidalgo and Taddei, 2014). Rainfall variability can be thought as resulting from two sources: one related to the oceanic-forcing and another one due to internal atmospheric processes and land–atmosphere interactions (e.g. Harzallah and Sadourny, 1995; Barreiro and Diaz, 2011). In this study, we will focus on the analysis of austral springtime rainfall variability over SESA related to the oceanically forced signal.

Recently, it has been shown that about 40% of SESA annual mean precipitation variability is caused by variations in the tropical sea surface temperatures (Seager *et al.*, 2010). The tropical oceans are known to influence rainfall variability in the subtropics through different mechanisms, including the generation of quasi-stationary Rossby waves that propagate to higher latitudes (e.g. Vera *et al.*, 2004) and anomalous changes in the Hadley and Walker regional cells (Ambrizzi *et al.*, 2004).

The link between El Niño-Southern Oscillation (ENSO) and precipitation over SESA (PCP) is historically strongest in austral spring, weaker in summer and stronger again in fall (Grimm *et al.*, 2000; Barreiro, 2010). The mechanisms through which El Niño influences rainfall over SESA involve both upper and lower-level atmospheric circulation anomalies. During El Niño the strengthening and meandering of the subtropical jet in upper-levels due to Rossby wave trains propagating from the equatorial Pacific increases the baroclinicity and the advection of cyclonic vorticity over SESA (Yulaeva and Wallace, 1994; Grimm *et al.*, 2000). In lower-levels the northerly flow from the Amazon basin strengthens, increasing the availability of moisture south of 20°S (Silvestri, 2004). This configuration enhances rainfall over SESA during a warm ENSO event. During high austral summer the subtropical jet moves poleward, weakening the upper level mechanism and the signal weakens. In the later austral summer the signal strengthens again and, if only El Niño events that last

* Correspondence to: V. Martín-Gómez, Instituto de Física, Facultad de Ciencias, Universidad de la República de Uruguay, Iguá 4225, Montevideo (Uruguay). E-mail: vero.martin.gomez@gmail.com

until the following May are considered, there is a significant positive anomaly in the region during fall that induces floods of the Parana river (Camilloni and Barros, 2003).

According to some studies, the tropical Atlantic influences precipitation over SESA mainly on multidecadal time scales while the tropical Pacific dominates the interannual band, together explaining most of the interannual to multidecadal variations (Seager *et al.*, 2010). Assuming linearity in the response, coexistence of an anomalously warm (cold) equatorial Pacific together with an anomalously cold (warm) Topical North Atlantic have been suggested to interact constructively to intensify persistent wet spells (drought periods) over subtropical South America (Mo and Berbery, 2011). Recently, a modelling study of Barreiro *et al.* (2014) found this ocean connection to increase rainfall over northern Argentina but not in other subtropical regions.

Some studies have presented evidence of a possible connection, which is not yet fully understood, between the tropical South Atlantic Ocean and precipitation over SESA. Diaz *et al.* (1998) found a simultaneous correlation between increased rainfall anomalies over SESA and warm anomalies off southeastern Brazil and the equatorial Atlantic during late spring and early summer. However, Robertson *et al.* (2003) found a very weak response on precipitation and surface temperature over SESA using model simulations forced with prescribed patterns of south Atlantic SST anomalies.

Other studies have shown that the Indian Ocean can also affect rainfall over South America. For example, Chan *et al.* (2008) showed that precipitation over subtropical La Plata Basin during austral spring increases when the Indian Ocean Dipole (IOD) is in positive phase, a connection mediated through a mid-latitude wave train that emanates from the tropical Indian Ocean and propagates to SESA. The authors propose that the associated low-level anomalous anticyclone located off the coast of Brazil intensifies the tropical easterlies and strengthens the South American Low-Level Jet, increasing the availability of moisture, thus favouring the anomalously high precipitation over Uruguay and northern Argentina.

In addition to influencing rainfall over SESA, these tropical oceans interact among each other inducing SST anomalies in remote basins through atmospheric and oceanic teleconnections. In the case of the Pacific–Atlantic teleconnection, there are observational (Enfield, 1996; Enfield and Mayer, 1997) and modelling studies (Harzallah *et al.*, 1996) which showed that ENSO has a significant remote influence on tropical Atlantic variability. The atmospheric teleconnection is established through anomalous surface heat fluxes as consequence of the changes in the trade winds and in the air–sea temperature difference associated with ENSO (Chiang and Sobel, 2002), in such a way that a warm Tropical North Atlantic (TNA) can be associated with positive SST anomalies in the eastern equatorial Pacific. The changes in the winds are established through the PNA teleconnection pattern induced by the tropical Pacific (e.g. Nobre and Shukla, 1996) and the largest response occurs during boreal spring (e.g. Enfield and Mayer, 1997; Saravanan and Chang 2000). The influence of the tropical Pacific on the Atlantic is, however, fragile and depends on the pre-existing SST conditions in the latter basin (Chang *et al.*, 2006). In turn, there are many studies suggesting a link in the opposite direction, that is, that temperature changes in the Atlantic Ocean can influence the equatorial Pacific (e.g. Dommenget *et al.*, 2006; Rodriguez-Fonseca *et al.*, 2009; Frauen and Dommenget, 2012; Yoo *et al.*, 2013).

The interaction between ENSO and the IOD is a controversial topic among the research community (Allan *et al.*, 2001). Some studies established that IOD events are a physical entity inherent to the Indian Ocean and can evolve without external forcing from the equatorial Pacific (Saji *et al.*, 1999; Webster *et al.*, 1999), but there are also other studies which showed that some IOD events can co-occur with El Niño and even be triggered by Pacific forcing (Annamalai *et al.*, 2003; Meyers *et al.*, 2007; Wang and Wang, 2014). These latter studies showed that the weakening of the Walker circulation induced by El Niño generates anomalous surface easterly winds that shallow the thermocline off Java-Sumatra and enhance the SST cooling via upwelling of anomalous cold water (Annamalai *et al.*, 2003; Wang and Wang, 2014).

There are also studies that investigate the impact of different El Niño events on the IOD separating El Niño into canonical El Niño (when the maximum SST anomalies are located in the eastern equatorial Pacific), and El Niño Modoki I and II (when the maximum SST anomalies are in the central equatorial Pacific). They show that while the canonical Niño and El Niño Modoki I are related to a positive IOD, El Niño Modoki II is associated with a negative IOD (Wang and Wang, 2014). It is also important to note that besides El Niño, there are other external drivers that can induce an IOD event, such as the Southern Annular Mode (Lau and Nath, 2004) and the monsoon (Fisher *et al.*, 2005).

To our knowledge there are no studies in the literature that show a direct influence of the TNA SST anomalies on the tropical Indian Ocean. However, there are studies which analyse the influence of SST anomalies in the Atlantic Ocean on the ENSO-Indian monsoon interaction (Kucharski *et al.*, 2007; Wang *et al.*, 2009) and directly on the Indian monsoon. For example, Goswami *et al.* (2006) showed that the increase of the meridional temperature gradient over the northern hemisphere during the positive phase of the Atlantic Multidecadal Oscillation (AMO) may extend the Indian monsoon, causing an increase of the seasonal mean Indian summer rainfall. The tropical SST expression of the AMO plays the dominant role in this teleconnection (Li *et al.*, 2008). At the same time, Li *et al.* (2003) showed that a strong Indian monsoon may change surface winds leading to cold SST anomalies in the western Indian Ocean (through enhanced surface evaporation, ocean mixing and coastal upwelling) and warm SST anomalies in the eastern Indian Ocean. Thus, the TNA may influence the Indian Ocean through changes in the monsoon.

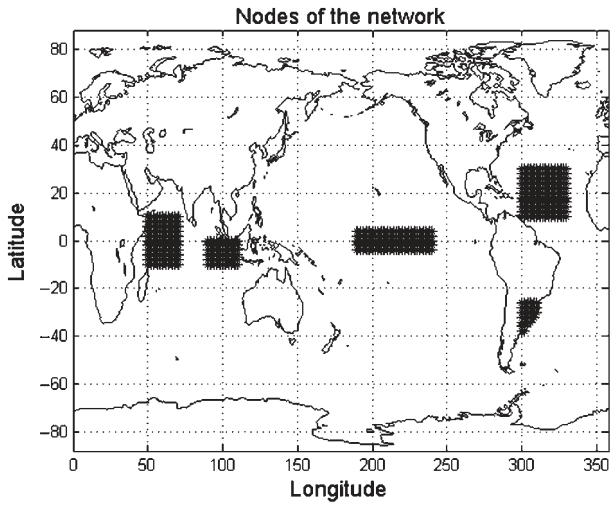

Figure 1. Regions that represents the climate indices: Indian Ocean Dipole (IOD) over the Indian Ocean, Niño3.4 over the central equatorial Pacific Ocean, the TNA and the precipitation over Southeaster South America (PCP).

All the aforementioned studies focus on the impact of a particular ocean basin (or a combination of two basins) on rainfall over SESA or on the surface ocean conditions of another basin. However, to our knowledge there is no study that addresses how the sea surface temperature anomalies in different basins interact to induce rainfall anomalies over SESA and neither how the interaction among oceans and their influence on rainfall variability has evolved with time. Thus, the goal of this study is to investigate the collective influence of the three tropical oceans (characterized by interannual phenomena) on precipitation over SESA and how this influence has evolved during the 20th century. We focus on the austral spring season because, as mentioned above, several previous studies have shown that it is during this season when rainfall over SESA is mostly influenced by the tropical oceans, exhibiting large variability on interannual to interdecadal time scales.

To address this issue we consider the interaction among oceans and their influence on SESA rainfall from a complex network perspective. We construct a climate network following the methodology of Tsonis *et al.* (2007) considering different indices that characterize the tropical oceans: El Niño/Southern Oscillation (Niño3.4), the TNA, and the IOD as well as an index that characterizes precipitation over SESA (PCP). These four climate indices will make up the nodes of the climate network (see Figure 1). We investigate the collective behaviour of the four network's nodes focusing on detection of synchronization events (when the network's nodes are most connected) and how this 'collective behaviour' has evolved with time. The synchronization events are defined considering the mean distance of cross-correlation. Thus, this methodology allows to detect periods when the tropical oceans are more connected and active in influencing rainfall over SESA.

The paper is organized as follows. In Section 2 we introduce the data and methodology used. In Section 3 we describe the main features of the network, compare observed and simulated results and define the synchronization periods that characterized the last century based on the mean network distance measure. Afterwards, we identify which nodes were significantly connected during synchronization periods. In Section 4 we discuss the possible physical mechanisms that characterized the interaction among the oceans and their influence on SESA rainfall. Finally, in Section 5 we summarize the results.

2. Data and methodology

2.1. Data

We define the different tropical oceanic indices considering the monthly mean SST data from 1901 to 2005 of two different datasets: ERSSTv3b (Extended Reconstructed Sea Surface Temperature; Smith *et al.*, 2008; Xue *et al.*, 2003) with a resolution of $2^\circ \times 2^\circ$, and HadSST (Hadley Center Sea Surface Temperatures; Rayner *et al.*, 2003) with a resolution of $1^\circ \times 1^\circ$. The Precipitation index is defined using the monthly mean observed data during the same period mentioned above from the GPCCv5 database (Global Precipitation Climatology Center; Schneider *et al.*, 2011) with a resolution of $1^\circ \times 1^\circ$. Table 1 summarizes the indices considered in this study.

We also consider the simulated precipitation field from an Atmospheric General Circulation Model (AGCM) forced with observed SST. In particular, we use the ICTP-AGCM (Molteni, 2003; Kucharski *et al.*, 2006) and construct an ensemble of 9 runs initializing the model with different atmospheric conditions, but all having the same SST as boundary conditions. The precipitation index is considered as the ensemble-mean precipitation over the region of interest (see Table 1) and by construction it will mainly represent the oceanically forced rainfall variability since, as several previous studies have shown, taking an ensemble of about 10 members is enough to filter out internal variability in most places (Saravanan and Chang, 2000; Barreiro and Tippmann, 2008; Barreiro, 2010). The ICTP-AGCM is forced with observed SST from the ERSSTv2 dataset. Smith *et al.* (2008) showed that ERSSTv2 and ERSSTv3 are very similar, which is further substantiated by the strong similarity of the indices used in this study according to Table 2. Thus, the main difference in the networks constructed using observed and simulated data will arise due to differences in the evolution of precipitation.

Given the larger similarity between ERSSTv2 and ERSSTv3b, the network constructed using the simulated rainfall will be mainly compared with the observed one constructed with ERSSTv3b. The network constructed with HadSST will be used to test the sensitivity of the network distance to observed SST.

2.2. Methodology

The methodology consists of several steps:

First, we construct the climate indices by latitudinal and longitudinally averaging SST and precipitation in the

Table 1. Geographical regions of each index that make up our network's nodes. The indices are constructed averaging the sea surface temperature or precipitation anomalies in the specified regions. In the Indian Ocean Dipole case, the index is constructed as from the difference between the average in the western region and the average in the eastern region. Regions are plotted in Figure 1.

Index short name	Long name index	Earth's region	
		Latitude range	Longitude range
NINO3.4	Niño3.4	5°N–5°S	170°W–120°W
TNA	Tropical North Atlantic	10°N–30°N	60°W–30°W
IOD	Indian Ocean Dipole	10°S–10°N	50°E–70°E
		10°S–0°N	90°E–110°E
PCP	Precipitation Southeastern South America (only land areas are considered)	40°S–25°S	60°W–50°W

Table 2. Pearson correlation coefficients between oceanic indices computed using ERSSTv3b and ERSSTv2.

Pearson correlation between each index from ERSSTv3b and the same index from ERSSTv2	Nino3.4	TNA	IOD
Pearson correlation coefficient	0.99	0.99	0.98

different regions considered (see Table 1 and Figure 1). We also eliminate the trend of the four time series and compute monthly anomalies, removing the climatological cycle from 1901 to 2005. In the case of the IOD, we subtract the average between the two boxes to construct the index. The indices are normalized by their respective standard deviations computed considering the period 1901–2005.

Second, we consider individual trimesters to construct the networks: September–November (SON) for the case of El Niño index and October–December (OND) for the rest of the indices (TNA, IOD and PCP). Before taking a 3-months mean and in order to avoid aliasing effects, we first apply a low-pass Lanczos Filter (Duchon, 1979) with cutoff frequency of 1/12 to the monthly mean time series. Therefore, the time series have 105 values, 1 per year.

As mentioned in the introduction, SESA precipitation in OND shows large variability on different time scales including interannual to interdecadal (Seager *et al.*, 2010). Also, it is during this season when the teleconnection between Niño3.4 and SESA precipitation is well established and when the IOD takes place and influences SESA precipitation variability (Li *et al.*, 2003; Chan *et al.*, 2008; Barreiro 2010). The literature mentioned in the introduction reveals that ENSO could induce SST anomalies in other tropical basins with a lag that varies from 1 to several months. Thus, we established a lag of 1 month between the Niño3.4 index and the rest of the network nodes to allow the Atlantic and Indian Oceans to respond to the atmospheric anomalies generated by the equatorial Pacific.

Third, following the methodology of Tsonis *et al.* (2007) we construct the network considering the mean network distance as synchronization measure. Mathematically, the mean network distance is defined as:

$$d(t) = \frac{2}{N(N-1)} \sum_{i<j} \sqrt{2\left(1 - \left|\rho_{ij}^{t}\right|\right)} \qquad (1)$$

where t denotes the time in the middle of a sliding window of width $\Delta t = 11$ years, N represents the number of network's nodes that we take into account to construct the climate network (in our case $N = 4$, TNA, IOD, PCP and Niño3.4) and ρ_{ij}^{t} is the cross correlation coefficient between nodes i and j in the interval $[t - (\Delta t/2), t + (\Delta t/2)]$. Note that to compute the mean network distance, for each sliding window we introduce the six values of the correlation coefficients that correspond to the six possible pairs of network's nodes, independently of whether they are significant or not because all of them contribute to the degree of synchronization of the network with higher or lower values of the distance. The time step for the sliding window is 1 year. The window length selected here is a compromise between being long enough to estimate correlations, but not too long for interdecadal variability modes to influence the behaviour. The observed synchronization periods are not very sensitive to a window size in the range of 9–13 years.

Climate teleconnections may in principle have a nonlinear nature. Nevertheless, Donges *et al.* (2009) and Arizmendi *et al.* (2014) showed that linear measures of similarity give very similar results as nonlinear measures, such as mutual information, when characterizing atmospheric teleconnection phenomena. Moreover, in our case the length of the sliding window precludes the computation of mutual information with enough reliability. Nonetheless, as a first order to test for nonlinearity, the network distance was also computed considering Spearman rank correlation. We found that the network distance is very similar independently on the correlation used except during the last decade of the 20th century, when the network distance computed with Spearman correlation does not show statistically significant synchronization among the network's nodes (Figure 2). This period includes the strong El Niño of 1997 which acts as an outlier strongly influencing Pearson correlation. The similarity in the evolution of both network distances during the first 90 years of the last century suggests that Pearson correlation is a valid measure of interdependence to represent climate teleconnections, and our study will be based on this correlation coefficient.

The mean network distance as a measure of synchronization is useful to study and describe the variations in the network's features. Note that the network is completely

synchronized when the distance is zero and disconnected when the distance is $\sqrt{2}$ (uncorrelated nodes). In turn, Equation (1) uses the absolute value of cross correlation because we are interested in the intensity of the interaction between the two nodes, which is independent of the correlation sign.

Fourth, to compute the statistical significance of the mean network distance we consider a Monte Carlo method employing the following criterion: we first compute the autocorrelation coefficient at lag 1 year of each index (remember that each index has one value per year and represents the seasonal mean), and consider as red noise those with autocorrelation coefficient significant at 95% level in a one-tailed *t*-test (white noise in the opposite case). Following this criterion, only the TNA can be considered as red noise, while the rest of the indices are white noise. Then, we generate 1000 surrogate time series of each index under these null hypotheses and compute the network distance time series considering a sliding window of 11-years length, as done for the observed indices. In this way, we construct 1000 surrogate time series of the mean network distance, which allows determining the 5% level. We consider that there is a statistically significant synchronization event when the mean network distance is below this threshold. This procedure is carried out considering the observed precipitation and the two observed SST datasets (ERSSTv3b and HadSST), as well as for the ICTP-AGCM's ensemble mean rainfall. We will see below that the network constructed with the model's output can reproduce the observed synchronization events. This means that the model reproduces well the observations and its output can be used to study the global circulation anomalies in each synchronization period.

3. Network's characteristics

In this section, we describe the main features of the network, compare the observed and simulated results, and define the synchronization periods that characterized the last century. Lastly, we determine which nodes had a statistically significant influence on SESA precipitation variability and how this changed from one synchronization period to another.

The characteristics of the network are studied using the time series of the mean network distance plotted in Figure 3. The solid, dash and square lines represent the mean network distance computed from ERSSTv3b, HadSST and ICTP-AGCM's outputs, respectively, and the horizontal black dot line is the threshold level.

3.1. Variability of the network distance and synchronization periods

The network distance is characterized by large interannual and interdecadal variability. There exist three periods in which the observed (ERSSTv3b and HadSST) and simulated (ICTP-AGCM) network distances computed using Pearson correlation evolve similarly and present synchronization (Figure 3). Focusing on the ERSSTv3b network

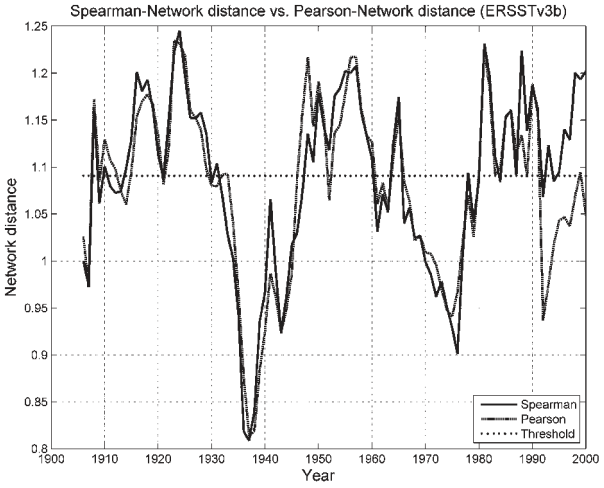

Figure 2. Network distance computed considering Spearman rank (solid line) and Pearson (dash line) correlations coefficients from ERSSTv3b indices. For each time step, the network distance is calculated considering the definition given by Tsonis et al., (2007) and a sliding window of 11 years length. El Niño index in centered on September–October–November (SON), and the rest of the indices on October–November–December (OND).

distance it is possible to distinguish that the first period occurs from 1933 to 1945 and the second period covers 1966–1978. The last synchronization period (during the 1990s) will not be considered since the mean network distance computed using the Spearman correlation does not show synchronization among the network's components (Figure 2, solid line).

To establish the synchronization periods we selected a period of years that fulfill two criteria: (1) the mean network distance is under the threshold level and (2) if we move the true window that represents the synchronization period 1 year to the left and 1 year to the right, the interacting nodes do not change (that is, the correlation coefficients that are statistically significant in the centered-window, remain statistically significant for the right/left moved-windows).

The fact that the two observed networks (solid and dash curves) evolve in a similar way during most of the period of study guarantees that the synchronization events do not depend on the chosen dataset. Nevertheless, the strength of the synchronization depends on the SST dataset used, being stronger for the ERSSTv3b (see first and second synchronization periods in Figure 3). Finally, it must be noted that during the first 30 years, the two observed datasets do not evolve in a similar way, which could be due to the scarcity of observations.

3.2. Relative weight of the nodes in synchronization periods

Overall, the time behaviour of the network distance calculated using simulated rainfall tends to follow the one constructed with observed rainfall (square and solid lines, Figure 3). However, while there are periods in which the amplitude of the simulated network distance (square line) is very similar to that using observations (e.g. first

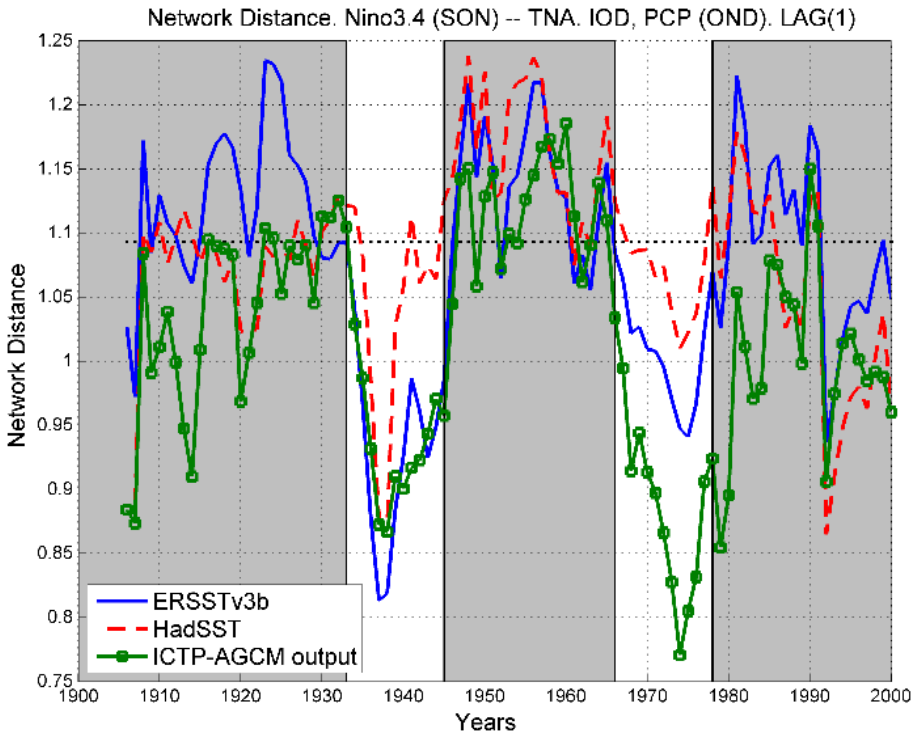

Figure 3. Network distance time series during the last 20th century. Solid, dash and square lines represent the mean distance computed from ERSSTv3b, HadSST and ICTP-AGCM's output, respectively. The horizontal dot - line line represents the threshold level. Whereas the ERSSTv3b and HadSST network distances are computed from the observed PCP index, the ICTP-AGCM network distance is computed from the PCP ensemble-mean. For each time step, the network distance is calculated considering the definition given by Tsonis *et al.* (2007) and a sliding window of 11 years length. El Niño index in centered on September–October–November (SON), and the rest of the indices on October–November–December (OND). The synchronization periods are marked by the white regions.

synchronization period), there are others in which this is not the case (e.g. the second synchronization period). As noted before, the main difference between the observed and simulated network distances should arise due to the precipitation index, because whereas in the simulated case the precipitation index contains mainly the oceanically forced component, the observed precipitation index contains both, the internal variability and oceanically forced signals. Moreover, model biases may also induce differences between observed and simulated precipitation.

To further analyse the representation of the network distance by the model, we compute the network distance for each one of the nine precipitation ensemble members of the experiment and define a confidence interval given by the maximum and minimum values for each 11 years window (Figure 4). Focusing on the ERSSTv3b-network distance (solid line in Figure 4), overall the observed network distance falls within the confidence interval except during the first synchronization period, but even then, it is possible to see that the observed and ensemble-mean simulated network distances are very close to each other. A similar situation occurs during 1957–1962. The only point where the behaviour could be considered different is 1923 when the observed network distance is out of the confidence interval and does not coincide with the simulated network distance. In any case, it is only one point and one that is not that important for our study because is not within a synchronization period.

Figure 4 also shows that in both synchronization periods the magnitude of the simulated network distance (dash line) is just outside the confidence interval, suggesting that large internal atmospheric variability within the ensemble is filtered out in the average procedure. By construction, the simulated network distance (dash line) can stay inside or under the confidence interval, but never above. This is because the ensemble-mean precipitation index has filtered most of the internal atmospheric variability signal, which would act as noise in the PCP time series decreasing in average the cross-correlation between the PCP index and any of the oceanic indices.

Looking more closely at the synchronization periods, in the first one the amplitude of the simulated and observed network distances is very similar. Such a result could be a consequence of SESA precipitation not being influenced by the tropical oceans. In this situation, the correlation coefficients between the tropical ocean indices and the precipitation would be close to zero and the similarity is obvious given that both (observed and simulated network distances) use observed SSTs. To check whether this is the case, we computed relative weights in order to determine the importance of individual nodes in the network. For example, for rainfall we define the relative precipitation weight (RPW) as:

$$\mathrm{RPW} = \frac{\left(\sqrt{2}/2\right) - d_{\mathrm{pcp}}}{\sqrt{2} - d} \qquad (2)$$

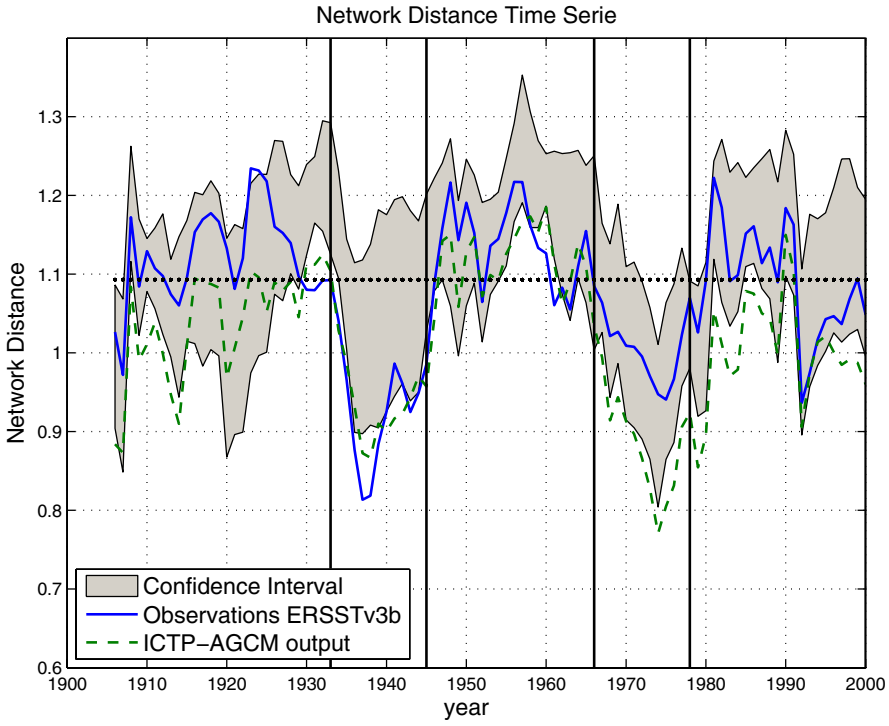

Figure 4. Simulated confidence interval for the network distance time series from 1901 to 2006 (shaded region). The solid and dash lines represent the observed and simulated network distance time series respectively. The observed network distance is calculated from ERSSTv3b dataset and the simulated considering the PCP from the ensemble mean.

where d_{pcp} represents the network distance calculated considering only the correlation coefficients between the precipitation index and the tropical ocean indices in Equation (1). The maximum and minimum values of the RPW are one and zero, respectively. Higher values of the RPW will be associated with larger influence of the tropical oceans on rainfall. RPW = 1 takes place when $d_{\text{pcp}} = 0$ (correlation coefficient between each one of the oceanic indices and the PCP index are 1 or −1) and the tropical oceans are completely disconnected among them. RPW = 0 means that SESA precipitation is completely disconnected from the tropical ocean indices $\left(d_{\text{pcp}} = \sqrt{2}/2\right)$. Analogously, it is possible to construct time series that describe the relative weight of each oceanic index.

Figure 5 shows the relative weight of each one of the network's nodes. The relative precipitation weight is represented by a solid line and shows relatively large values during the first synchronization period (1933–1945), suggesting that the tropical oceans influence SESA precipitation. In fact, the mean value of the RPW = 0.58 represents the second largest value of node's relative weights during this period (after Niño3.4 index, see Table 3). Comparing the values of the relative weight of each index during this period it is clear that Niño 3.4 was the most connected node of the network, followed closely by SESA precipitation (see Table 3). Thus, precipitation has high correlation values with the other network's nodes and the fact that the magnitude of the network distance simulated by the model follows the observed ones (see Figure 3 or 4) suggests that the oceanically forced signal on rainfall was strong during this period and the ensemble-mean precipitation represents it correctly.

During the second synchronization period observed and simulated network distances have different magnitudes. In this period the observed network distance is well within the confidence interval, suggesting a weak oceanically forced signal embedded in large internal atmospheric variability. As before, Niño3.4 is the most connected network's node, but now the IOD is as important as the PCP index (see Table 3). In comparison with the 1930s, the connectivity of SESA precipitation index decreases in the 1970s (and the RPW shows a relative minimum, Figure 5). Also, we can see that whereas the IOD has high weight in the network during the second synchronization period, the weight of the TNA is slightly larger in the first period (see Table 3). Finally, if we focus on the mean values of the relative weights computed over the whole 20th century, Niño3.4 was the most connected network's node, followed by the PCP, IOD and TNA indices (see Table 3), suggesting that ENSO has a vital importance in the global network. In turn, from the correlation values of the tropical ocean indices and SESA precipitation it is clear that the equatorial Pacific is the node that had strongest influence on rainfall variability over SESA during the last century (see Table 4) which is consistent with the literature.

Lastly, it is important to note that a large relative weight of rainfall does not necessarily translate into a small network distance, as happened during 1955–1965. This suggests that during this period the interaction among the oceans is weak.

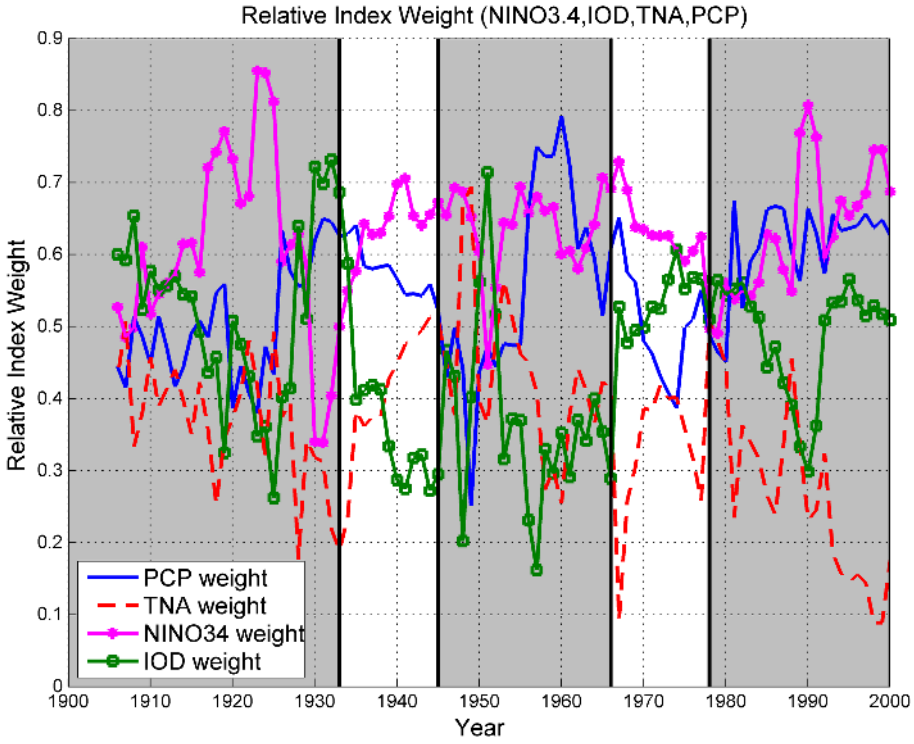

Figure 5. Relative Index time series. This parameter indicates the importance of the each node in the network and is enclosed between zero and one. Higher values of the relative weight are associated with higher importance of the particularly index in the network. We compute this parameter considering the observed data from ERSSTv3b. The synchronization periods are marked with the white regions.

Table 3. Mean of the relative weight during 1930s, 1970s and whole the 20th century together with the corresponding standard deviations for each network's node.

Relative weight	Mean 1930s	Std 1930s	Mean 1970s	Std 1970s	Mean 20th	Std 20th
PCP	0.58	0.04	0.51	0.08	0.55	0.10
TNA	0.41	0.10	0.35	0.10	0.36	0.12
IOD	0.39	0.13	0.52	0.08	0.46	0.12
NINO3.4	0.61	0.06	0.63	0.06	0.63	0.09

Table 4. Pearson correlation values between each one of the oceanic indices and SESA precipitation over whole the 20th century. At 95% significant level in a one-tailed t-test, the threshold level is: 0.16.

	NINO3.4-PCP	TNA-PCP	IOD-PCP
Pearson correlation	0.64	0.14	0.38

3.3. Relationship with modes of interdecadal variability

Given the large interdecadal variability of the network distance, we considered the possibility that it could be related to known interdecadal variability phenomena, in particular to the Atlantic Multidecadal Oscillation (AMO) and the Pacific Decadal Oscillation (PDO). To address this issue, we computed the correlation coefficient between these phenomena and the network distance obtained using the ERSSTv3b dataset. We use the monthly values of the PDO and AMO indices from 1901 to 2005 obtained from http://jisao.washington.edu/pdo/ and http://www.esrl.noaa.gov/psd/data/timeseries/AMO/, respectively. As done for the oceanic and rainfall indices, we remove the trend, compute monthly anomalies and apply a Lanczos filter to the time series of PDO and AMO. Afterwards, we average the values of October–November–December to obtain the PDO and AMO indices 105 years long. Finally, we take a sliding window of 11 years length and calculate the average of the PDO and AMO values inside each sliding window. This procedure results in two time series (one for PDO index and another for AMO index) of 95 values which are correlated with the ERSSTv3b network distance. It is found that the behaviour of the mean network distance is not significantly correlated with AMO, but it presents significant correlation with the PDO at the 95% significance level based on a Monte Carlo approach (correlation value is −0.22 and the threshold level is 0.21), suggesting that the synchronization of the network's components has a certain dependency with the evolution of the PDO. From visual inspection (Figure 6), it is possible to distinguish two distinct periods of different behaviour between

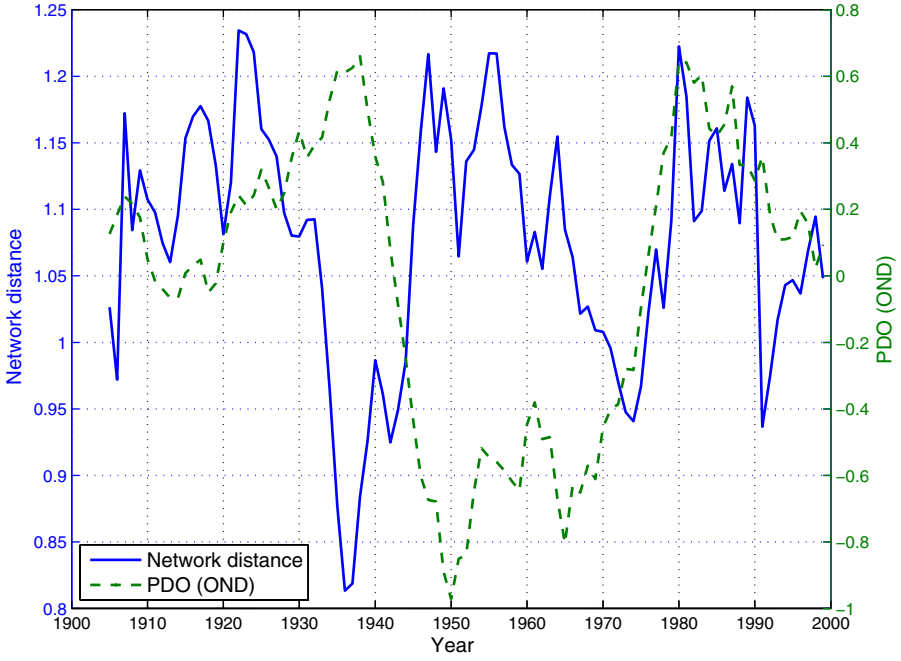

Figure 6. Evolution of the network distance time series computed from the observed ERSSTv3b dataset (solid line) and PDO index (dash line) during the last century.

the PDO and the network distance: whereas before the mid-70s both time series evolved with opposite phases, after the mid-70s they evolved in phase. If we consider the first 70 years of the period, the cross-correlation between PDO and the mean network distance is −0.37, statistically significant at 95% significance level based on a Monte Carlo approach. The correlation coefficient for the last 30 years is not computed given the uncertainty in the behaviour of the network distance in the 1990s (Figure 2). Note that the first synchronization period (1933–1945) coincides with a maximum of the PDO index, while the second period does not seem to coincide with extremes in the PDO. Thus, the role of the PDO in the network behaviour is not clear and more work is needed to elucidate its role. One possibility would be to include it as an additional node of the network in future studies. The AMO, on the other hand, does not seem to play a role.

3.4. Node connection during synchronizations

Up to this point we have found that during the 20th century there were two synchronization periods: (1933–1945) and (1966–1978). The following step is to determine which nodes were 'actually connected', that is, interacting among each other during each synchronization period. Although the mean network distance was computed considering the correlation of the six possible pairs of network's nodes, because all of them contribute to the degree of synchronization of the network, this does not mean that the six possible pairs always present statistically significant correlations. Two nodes will be 'actually connected', and therefore interacting between each other, if the correlation coefficient is statistically significant. Therefore, to determine which nodes were actually interacting, we compute the Pearson correlation coefficients between each pair of network's nodes during each synchronization period considering model simulations and check their statistical significance using a Monte Carlo method based on the generation of 10 000 surrogates time series. Surrogates of each index are constructed by random permutation taking blocks of one element (value) of the time series for the case of the Niño3.4, IOD and PCP, and blocks of two values of the time series for the case of the TNA index in order to maintain the observed serial autocorrelation (i.e. to preserve the observed red noise behaviour of the TNA index). The criterion that establishes if two network nodes are interacting is the following: (1) We first take a period ('window') that corresponds with the years in which the network distance is under the threshold level in Figure 4 and compute all the correlation coefficients between the network's nodes. (2) Afterwards, we move the centered-window 1 year to the left and 1 year to the right, and compute again the correlation coefficients among the nodes for each moved-window (see Tables 5 and 6). We say that two nodes are interacting if the three values of the cross-correlation remain statistically significant. According to this procedure for the second synchronization period we will not consider the interaction of PCP-TNA as a network link, since the interaction between both nodes does not remain significant for the three windows considered (see Table 6).

Tables 5 and 6 show that even though all nodes have at least one connection in each synchronization period, the characteristics of the network are different. During the 1930s, Niño3.4 is connected to all the rest of the nodes and there is a link between PCP and TNA. During the 1970s, Niño3.4 is also connected to all the nodes, but the PCP became connected to the IOD. From the point

Table 5. Pearson correlation coefficients for the different windows that represent the first synchronization period. Threshold level: 0.48 at 95% significant level in a Monte Carlo test based on the generation of 10 000 surrogate time series.

Pearson correlation threshold: 0.48	(1932–1944)	(1933–1945)	(1934–1946)
NINO3.4-PCP	0.68	0.70	0.69
NINO3.4-TNA	0.68	0.68	0.67
NINO3.4-IOD	0.72	0.72	0.57
IOD-TNA	0.19	0.18	−0.04
IOD-PCP	0.12	0.11	−0.02
PCP-TNA	0.92	0.93	0.87

Table 6. Same as Table 5, but for the second synchronization period.

Pearson correlation threshold: 0.48	(1965–1977)	(1966–1978)	(1967–1979)
NINO3.4-PCP	0.86	0.88	0.88
NINO3.4-TNA	0.60	0.57	0.59
NINO3.4-IOD	0.56	0.61	0.61
IOD-TNA	0.35	0.36	0.38
IOD-PCP	0.65	0.66	0.66
PCP-TNA	0.47	0.46	0.51

of view of precipitation over SESA, during the 1930s the equatorial Pacific and the TNA dominated the oceanically forced component of the variability. On the other hand, during the 1970s the TNA does not play a role, and the Indian Ocean becomes connected to rainfall over SESA, in addition to the Pacific. This result can also be observed in Figure 7(a) and (c), which represent the correlation map between the PCP index and the sea surface temperature anomalous field in each synchronization period, indicating the regions of the ocean that influence rainfall variability over SESA.

In the following section we hypothesize the possible physical mechanisms that characterized the interaction among the nodes of the network important for rainfall over SESA during synchronization periods based on the literature. We employ the ICTP-AGCM's output since, as we saw, this model reproduces well the observations and allows to better characterize the oceanically forced atmospheric circulation anomalies.

4. Discussion

4.1. Period (1933–1945)

The oceanic nodes that had an important role on rainfall variability during the period 1933–1945 are Niño3.4 and the TNA (see Figure 7(a)).

Link Niño3.4-TNA: There are two different processes through which a warm anomaly in the equatorial Pacific can influence the TNA: a weakening of the trades which decreases the oceanic heat loss (e.g. Enfield and Mayer, 1997) and the tropospheric temperature warming bridge (Chiang and Sobel, 2002). The regression maps onto Niño3.4 show a small warming of the TNA accompanied by weak decreased trades (Figure 8(a) and (c)). The small TNA response might be a consequence of the small time lag allowed for the ocean response (1 month), instead of a typical scale of one season (e.g. Enfield and Mayer, 1997; Saravanan *et al.*, 2000).

Link Niño3.4-PCP: As mentioned in the introduction, the mechanisms through which El Niño influences SESA involve both upper and lower-level atmospheric circulation anomalies. In upper-levels the Rossby wave trains propagating from the equatorial Pacific increase the baroclinicity and the advection of cyclonic vorticity over the region (Yulaeva and Wallace, 1994; Grimm *et al.*, 2000). This can be observed in the regression map of the geopotential height onto the Niño3.4 index (Figure 8(b)), which shows the presence of a through-ridge system over subtropical South America. At the same time, in lower-levels there is an increase of the northerly transport of moisture into the region because of a strengthening of the southward wind (Figure 8(d), in agreement with Silvestri, 2004). The combination of these two factors favours an increase of precipitation over SESA.

Regarding the interaction between the TNA and PCP, it is important to note that the correlation is approximately 0.9, larger than the one between PCP and Niño3.4. Also even after El Niño signal is removed (Figure 7(b)), the SST anomaly in the TNA is still significantly correlated with rainfall over SESA. This suggests that the link between TNA and PCP is direct and that the SST anomalies in the TNA cannot be completely explained by ENSO forcing. To look at the influence of TNA directly onto SESA we performed partial regression maps of geopotential height and velocity potential at 300mb as well as of meridional wind at 850mb onto the TNA index maintaining Niño3.4 index constant (Figure 9(b)–(d)). We found that in upper-levels the geopotential height shows a trough over SESA favouring the upward motions over this region. At the same time, there is upper-level divergence over the TNA and convergence over the Amazon Basin (Figure 9(c)). In lower-levels Figure 9(d) shows strong northward anomalous winds over the TNA and southward low-level winds over subtropical South America. These anomalies in upper-level divergence and surface winds suggest that the mechanism proposed by Yoon and Zeng (2010) is acting. They find that a warm TNA induces anomalous convergence of low level winds, upward vertical motion and divergence aloft. This divergent circulation results in anomalous convergence at upper-levels over the Amazon Basin and divergence at the surface that reduces rainfall there and strengthens the northerly winds that transport moisture towards SESA (Figure 5 from Yoon and Zeng, 2010). However, in our results the anomalies are not significant over the region and further work is needed to understand the influence of the TNA on rainfall over SESA. Nevertheless, these results allow to hypothesize that the combined influence of these two tropical indices (Niño3.4 and TNA) on SESA precipitation is such that a warm TNA in conjunction with a warm equatorial Pacific may favour a larger increase in the northerly winds that

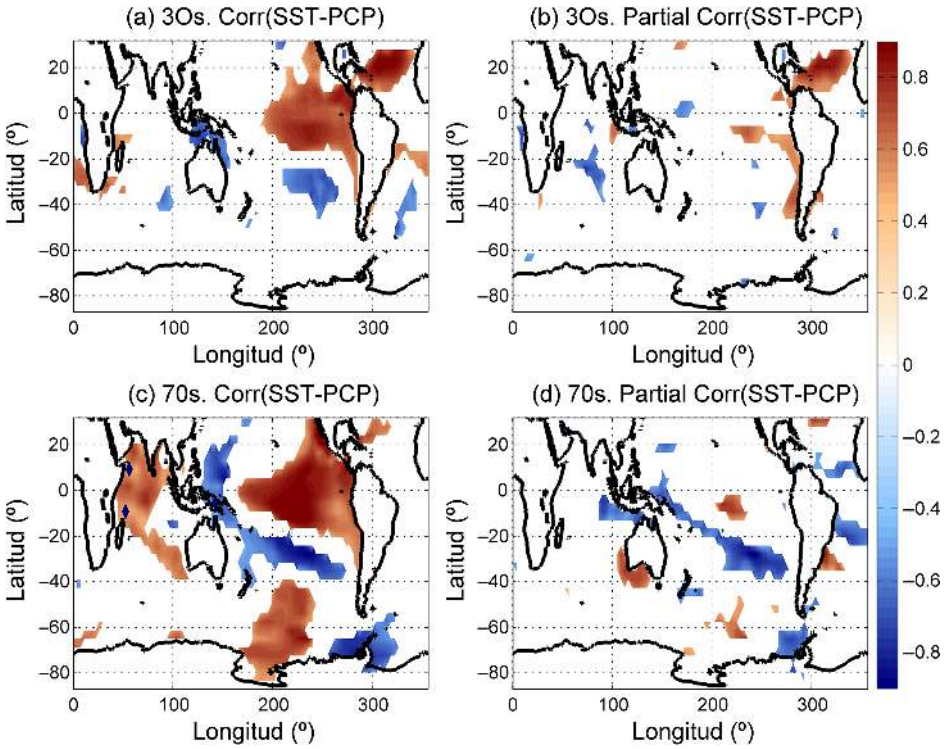

Figure 7. Correlation maps between precipitation index (OND) and the sea surface temperatures anomalies centered on OND: (a) in the 1930s and (c) in the 1970s. Partial cross correlation maps between precipitation index (OND) and the sea surface temperatures anomalies centered on OND maintaining Niño3.4 index (SON) constant: (b) in the 1930s and (d) in the 1970s. These maps were computed considering ICTP-AGCM output. Shown values exceed 95% level of confidence from one-tailed *t*-test.

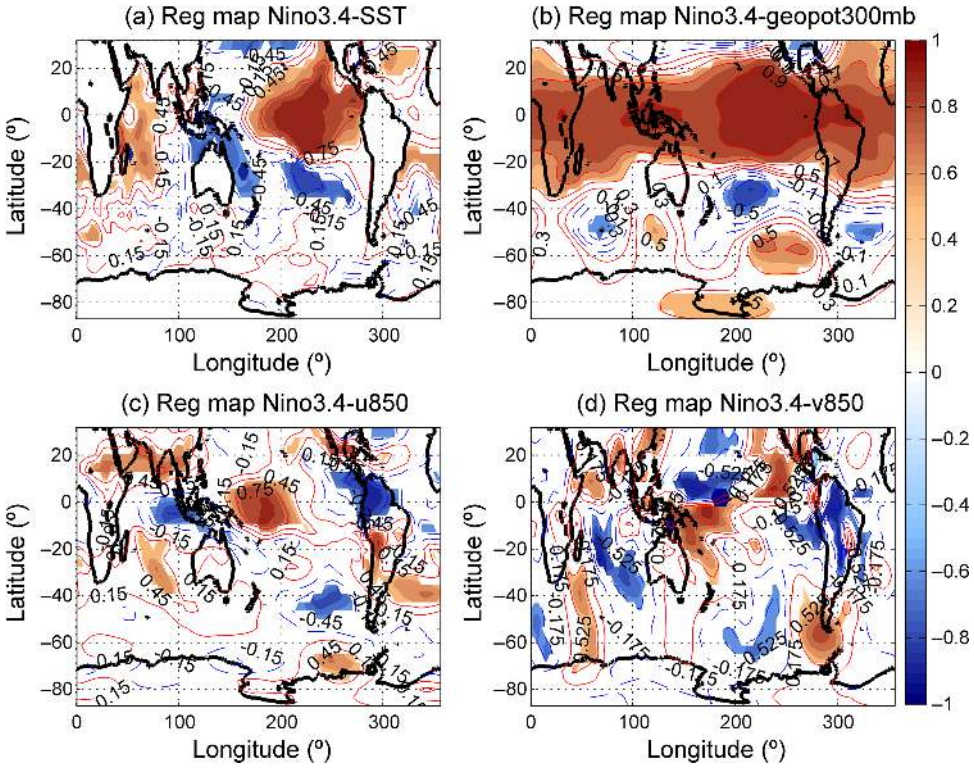

Figure 8. Regression map of the El Niño3.4 index (centered on SON) with: (a) sea surface temperatures anomalies, (b) geopotential height 300mb (geopot300mb), (c): zonal wind anomalies in 850mb (u850) and (d) meridional wind in 850mb (v850). The SST, geopot300, u850 and v850 are centered on OND. First synchronization period (1933–1945). Shaded regions represent values higher than 95% confidence level for one-tailed *t*-test. Maps computed from the ICTP-AGCM outputs.

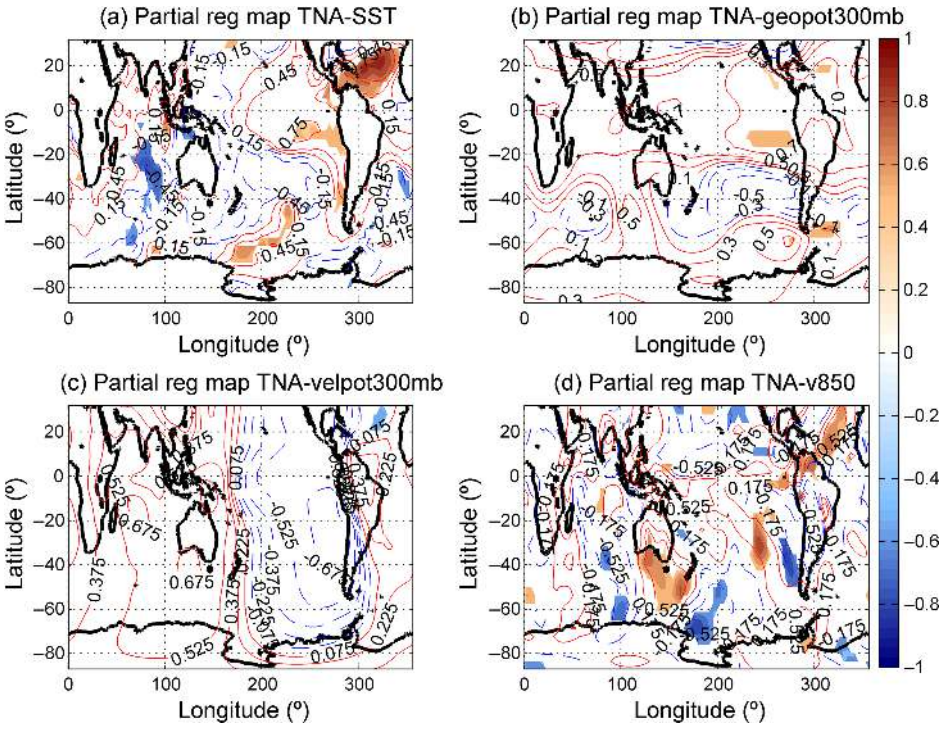

Figure 9. Regression map of the TNA index (centered on OND) with: (a) sea surface temperatures anomalies, (b) geopotential height 300mb (geopot300mb), (c) velocity potential at 300mb (velpot300mb), (d): meridional wind at 850mb (v850). The SST, geopotential height, velocity potential and v850 are centered on OND. First synchronization period (1933–1945). Shaded regions represent values higher than 95% confidence level for one-tailed *t*-test. Maps computed from ICTP-AGCM output.

bring moisture from the Amazon towards SESA, thus further increasing rainfall there.

4.2. Period (1966–1978)

In this case, the oceanic nodes that had an important role on rainfall variability are Niño3.4 and the IOD (see Figure 7(c)).

Link Niño3.4-PCP: The interaction between El Niño and the precipitation over SESA is similar to the previous case since the two favourable conditions to the increase for precipitation over the region of study are present (Figure 10(b) and (d)).

Link IOD-PCP: In this period the IOD appears like an important network's node, having a significant link with the PCP node (Figure 7(c)). This link would suggest an influence of the Indian Ocean on rainfall in SESA. However, the partial cross – correlation map between the precipitation index and the sea surface temperatures field maintaining the Niño3.4 index constant (Figure 7(d)), shows that the correlation between the PCP and SST over the Indian Ocean is not significant, suggesting that the appearance of this link could be due to the fact that both nodes have a common forcing: El Niño. Another possibility is that the Indian Ocean warming, as consequence of the Pacific forcing, influenced the rainfall over SESA through the eastward propagation of Rossby waves, a mechanism already proposed by Saji *et al.* (2005) and Chan *et al.* (2008). In fact, the regression map of 300mb geopotential height shows significant anomalies in the southeastern Indian Ocean and the extratropical atmosphere (Figure 10(b)) that were barely present in the 1930s (Figure 8(b)). This Rossby wave train may interact with the one forced by the tropical Pacific, and together may favour better conditions for increased precipitation over SESA (in agreement with the previous works of Saji *et al.*, 2005; Chan *et al.*, 2008).

Link Niño3.4-IOD: The connection between both oceans (equatorial Pacific and Indian) is established through anomalous winds (Annamalai *et al.*, 2003; Wang and Wang, 2014). During the 1970s, the regression map of the Niño3.4 index and the 850mb zonal wind (Figure 10(c)) shows negative anomalies of the zonal wind over the western shore of Sumatra that favours upwelling and contributes to decreasing the SST, and positive anomalies over the Arabian Sea and Bay of Bengal facilitating the homogeneous increase of the SST there. Nevertheless, during this period the Indian Ocean warms rather homogeneously presenting a weak east–west SST gradient (Figure 10(a)).

5. Summary

Several studies have shown that the tropical Pacific, Atlantic and Indian Oceans influence rainfall variability over SESA. Furthermore, these tropical oceans interact with each other forcing sea surface temperature anomalies in remote basins through atmospheric and oceanic teleconnections. However, it is not yet clear how these sea surface temperature anomalies in different basins interact together to induce austral spring rainfall variability over SESA and neither how the interaction among the

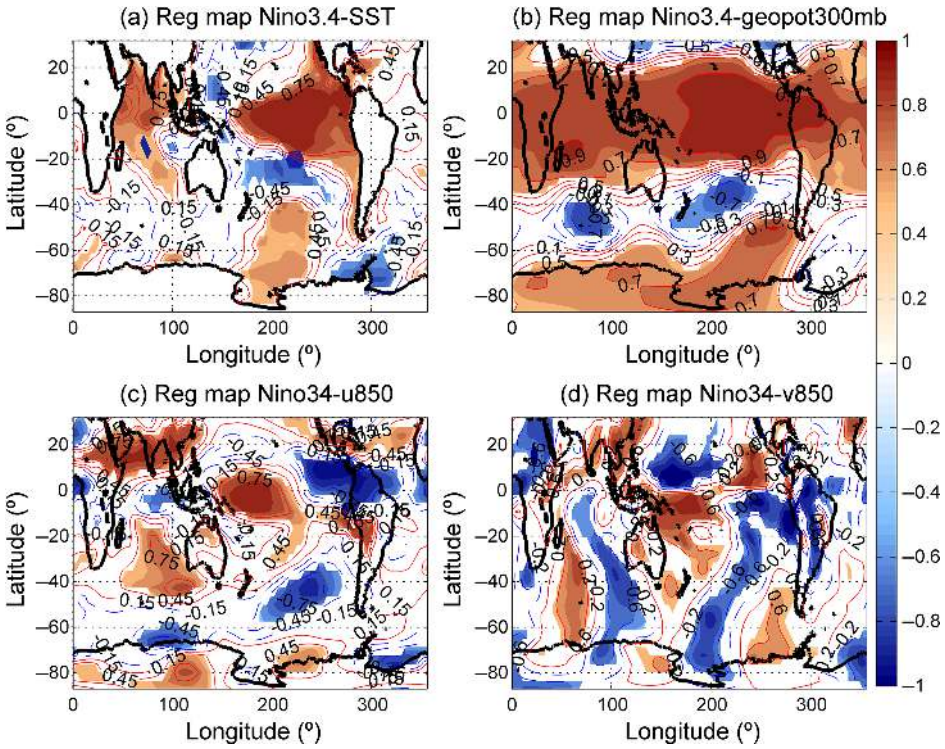

Figure 10. Regression map of the El Niño3.4 index (centered on SON) with: (a) sea surface temperatures anomalies, (b) geopotential height 300mb (geopot300mb), (c) zonal wind anomalies in 850mb (u850) and (d) meridional wind in 850mb (v850). The SST, geopot300, u850 and v850 are centered on OND. Second synchronization period (1966–1978). Shaded regions represent values higher than 95% confidence level for one-tailed *t*-test. Maps computed from the ICTP-AGCM outputs.

tropical oceans and their influence on rainfall variability has evolved with time. This work addresses these issues studying the collective behaviour of the tropical oceans and that of the precipitation over SESA and how this behaviour has evolved during the last century.

Following the methodology of Tsonis *et al.* (2007) we have constructed a network considering as nodes three oceanic indices that characterize the interannual variability of the tropical oceans (Niño3.4, IOD and TNA) as well as an index that characterizes the precipitation over SESA (PCP). We studied the network's characteristics and the collective behaviour of the nodes through the detection of synchronization events considering the mean network distance as a measure of synchronization among the nodes.

We computed the network distance considering two different observed datasets (ERSSTv3b and HadSST) to guarantee that the observed synchronization events do not depend on the chosen dataset. In addition, after checking that the ICTP-AGCM reproduces well the observed behaviour, we considered its output to study the global circulation anomalies that connect the different oceans and rainfall in the region of interest.

The main results of the study are as follows:

(1) Overall, we were able to show that the network distance presents interannual and interdecadal variability and could identify two synchronization periods during the last century. The first is from 1933 to 1945 (1930s) and the second covers 1966–1978 (1970s). A third potential synchronization period was detected during the 1990s, but its existence depends on the correlation measure used and was not further studied.

(2) The connectivity among the nodes in the network changed with time. Whereas in the first synchronization period the nodes with significant influence on precipitation in SESA were Niño3.4 and TNA, in the second they were Niño3.4 and IOD. Moreover, it was shown that a positive phase of the IOD and positive SST anomalies in the equatorial Pacific and TNA oceans induce positive SESA precipitation anomalies (Tables 5 and 6, Figure 7(a) and (c)).

(3) ENSO is shown to influence SESA precipitation variability during the two synchronization periods. The influence is such that the positive phase of ENSO induces positive rainfall anomalies over SESA and it could be understood through an increase of the northerly transport of moisture in lower-levels and the advection of cyclonic vorticity in upper-levels (in agreement with Yulaeva and Wallace, 1994; Grimm *et al.*, 2000; Silvestri (2004)).

(4) Regarding the interaction between the TNA and PCP during the 1930s, it is important to note that even after the El Niño signal is removed, the TNA is significantly correlated with rainfall over SESA. This suggests that the link between TNA and PCP is direct and the SST anomalies in the TNA cannot be completely explained by ENSO forcing. The TNA could impact precipitation over SESA through changes in

the regional divergent circulation and northerly surface winds as proposed by Yoon and Zeng (2010). Interestingly, the standard deviation of the TNA (not shown) shows that the period of maximum value coincides with the first synchronization period. Nevertheless, regression maps onto TNA do not show significant low-level circulation anomalies, so further work is needed to elucidate the influence of the TNA on rainfall over SESA.

(5) There are two possible, not mutually exclusive ways, of interpreting the interaction between the IOD and PCP. One possibility is that the appearance of this link is due to the fact that both nodes (IOD and PCP) are forced by El Niño. Another possibility is that the Indian Ocean warming increases rainfall over SESA through the eastward propagation of Rossby waves (in agreement Saji *et al.*, 2005; Chan *et al.*, 2008).

(6) Finally, regarding the combined influence of the tropical oceans on SESA precipitation during each synchronization period, we hypothesize that during the first synchronization period a warm TNA in conjunction with a warm equatorial Pacific may favour a larger increase in the northerly winds that bring moisture from the Amazon towards SESA, thus further increasing rainfall there. As for the second synchronization period, we hypothesize that a Rossby wave train induced by the Indian Ocean could interact with the one forced by the tropical Pacific, so that together may favour better conditions for increased precipitation over SESA through, e.g. an increase in the advection of cyclonic vorticity in upper-levels.

This study focuses on precipitation variability consequence of the combination of remotely forced teleconnections from the tropical Pacific, Atlantic and Indian Oceans, keeping in mind that these are the main phenomena that add predictability to rainfall. We have not included the tropical south Atlantic, because it is not clear to date whether it influences SESA precipitation, even though some studies have shown correlations (e.g. Diaz *et al.*, 1998; Robertson *et al.*, 2003). We plan, in a future work, to add the tropical South Atlantic as a network node. In addition, indices for soil moisture and the strength of the South Atlantic Convergence Zone and Amazon rainfall could be added to the network.

Overall, our results suggest a complex dynamics among the tropical oceans and their influence on rainfall over SESA that varies on interannual and interdecadal time scales. The complex network perspective used here has allowed to gain new insights in their collective behaviour, and resulted in new questions that need to be addressed in future studies.

Acknowledgements

The research leading to these results has received funding from the European Community's Seventh Framework Programme [FP7/2007-2011] under grant agreement no. 289447 (ITN LINC).

References

Allan RJ, Chambers D, Drosdowsky W, Hendon H, Latif M, Nicholls N, Smith I, Stone R, Tourre Y. 2001. Is there an Indian Ocean dipole, and its independent of the El Niño-Southern Oscillation? *Clivar Exchanges* **6**(3): 18–22.

Ambrizzi T, de Souza EB, Pulwarty RS. 2004. The Hadley and Walker regional circulations and associated ENSO impacts on South American seasonal rainfall. In *The Hadley Circulation: Present, Past and Future*, Diaz HF, Bradley RS (eds). Springer: Dordrecht, The Netherlands, 203–235.

Annamalai H, Murtugudde R, Potemra J, Xie SP, Liu P, Wang B. 2003. Coupled dynamics over the Indian Ocean: spring initiation of the zonal mode. *Deep Sea Res. II Trop. Stud. Oceanogr.* **50**(12): 2305–2330.

Arizmendi F, Martí AC, Barreiro M. 2014. Evolution of atmospheric connectivity in the 20th century. *Nonlinear Process. Geophys.* **21**(4): 825–839.

Baethgen WE, Magrin GO. 2000. Applications of climate forecasts in the agricultural sector of South East South America. In *Climate Prediction and Agriculture*, *Proceedings of the START/WMO International Workshop*, Geneva, Sivakumar MVK (ed). International START Secretariat: Washington, DC, 248–266.

Barreiro M. 2010. Influence of ENSO and South Atlantic Ocean on climate predictability over southeastern South America. *Clim. Dyn.* **35**: 1493–1508, doi: 10.1007/s00382-0666-9.

Barreiro M, Diaz N. 2011. Land-atmosphere coupling in El Nino influence over South America. *Atmos. Sci. Lett.* **12**: 351–355, doi: 10.1002/asl.348.

Barreiro M, Tippmann A. 2008. Atlantic modulation of El Nino influence on summertime rainfall over Southeastern South America. *Geophys. Res. Lett.* **3**: L16704, doi: 10.1029/2008GL035019.

Barreiro M, Diaz N, Remon M. 2014. Role of the global oceans and land-atmosphere interaction on summertime interdecadal variability over northern Argentina. *Clim. Dyn.* **42**(7–8): 1733–1753, doi: 10.1007/s00382-014-2088-6.

Camilloni IA, Barros VR. 2003. Extreme discharge events in the Parana River and their climate forcing. *J. Hydrol.* **278**(1): 94–106.

Chan SC, Behera SK, Yamagata T. 2008. Indian Ocean Dipole influence on South American rainfall. *Geophys. Res. Lett.* **35**(14): L14S12, doi: 10.1029/2008GL034204.

Chang P, Fang Y, Saravanan R, Ji L, Seidel H. 2006. The cause of the fragile relationship between the Pacific El Niño and the Atlantic Niño. *Nature* **443**: 324–328, doi: 10.1038/nature05053.

Chiang JC, Sobel AH. 2002. Tropical tropospheric temperature variations caused by ENSO and their influence on the remote tropical climate. *J. Clim.* **15**: 2616–2631.

Diaz AF, Studzinski CD, Mechoso CR. 1998. Relationships between precipitation anomalies in Uruguay and southern Brazil and sea surface temperature in the Pacific and Atlantic Oceans. *J. Clim.* **11**(2): 251–271.

Dommenget D, Semenov V, Latif M. 2006. Impacts of the tropical Indian and Atlantic Oceans on ENSO. *Geophys. Res. Lett.* **33**(11): L11701, doi: 10.1029/2006GL025871.

Donges JF, Zou Y, Marwan N, Kurths J. 2009. Complex networks in climate dynamics. *Eur. Phys. J. Spec. Top.* **174**(1): 157–179.

Duchon CE. 1979. Lanczos filtering in one and two dimensions. *J. Appl. Meteorol.* **18**: 1016–1022.

Enfield DB. 1996. Relationships of inter-American rainfall to tropical Atlantic and Pacific SST variability. *Geophys. Res. Lett.* **23**: 3305–3308, doi: 10.1029/96GL03231.

Enfield DB, Mayer DA. 1997. Tropical Atlantic sea surface temperature variability and its relation to El Niño Southern Oscillation. *J. Geophys. Res. Oceans* **102**: 929–945, doi: 10.1029/96JC03296.

Fisher AS, Terray P, Guilyardi E, Gualdi S, Delecluse P. 2005. Two independent triggers for Indian Ocean dipole mode in a coupled GCM. *J. Clim.* **18**: 3428–3449.

Frauen C, Dommenget D. 2012. Influences of the tropical Indian and Atlantic Oceans on the predictability of ENSO. *Geophys. Res. Lett.* **39**(2): L02276, doi: 10.1029/2011GL050520.

Goswami BN, Madhusoodanan MS, Neema CP, Sengupta D. 2006. A physical mechanism for North Atlantic SST influence on the Indian summer monsoon. *Geophys. Res. Lett.* **33**(2): L02706, doi: 10.1029/2005GL024803.

Grimm AM, Barros VR, Doyle ME. 2000. Climate variability in Southern South America associated with El Niño and La Niña events. *J. Clim.* **13**(1): 35–58.

Harzallah A, Sadourny R. 1995. Internal versus SST-forced atmospheric variability as simulated by an atmospheric general circulation model. *J. Clim.* **8**(3): 474–495.

Harzallah A, Rocha de Aragao JO, Sadourny R. 1996. Interannual rainfall variability in North-East Brazilo: observation and model simulation. *Int. J. Climatol.* **16**: 861–878.

Hidalgo C, Taddei R. 2014. Sustainable decisions and provision of climate services to the agriculture and water sectors of southeastern South America. In *WCRP Conference for Latin America and the Caribbean: Developing, Linking and Applying Climate Knowledge*, Montevideo, 14–17 March.

Kucharski F, Molteni F, Bracco A. 2006. Decadal interactions between the western tropical Pacific and the North Atlantic Oscillation. *Clim. Dyn.* **26**: 79–91.

Kucharski F, Bracco A, Yoo JH, Molteni F. 2007. Low-frequency variability of the Indian monsoon-ENSO relationship and the tropical Atlantic: the "weakening" of the 1980s and 199s. *J. Clim.* **20**: 4225–4266.

Lau NC, Nath MJ. 2004. Coupled GCM simulation of atmosphere ocean variability associated with the zonally asymmetric SST changes in the Tropical Indian Ocean. *J. Clim.* **17**: 245–265.

Li T, Wang B, Chang CP, Zhang Y. 2003. A theory for the Indian Ocean dipole-zonal mode. *J. Atmos. Sci.* **60**: 2119–2137.

Li S, Perlwitz J, Quan X, Hoerling MP. 2008. Modeling the influence of North Atlantic multidecadal warmth on the Indian summer rainfall. *Geophys. Res. Lett.* **35**(5): L05804, doi: 10.1029/2007GL032901.

Meyers G, Mcintosh P, Pigot L, Pook M. 2007. The years of El Niño, La Niña and interactions with the tropical Indian Ocean. *J. Clim.* **20**: 2872–2880.

Mo KC, Berbery EH. 2011. Drought and persistence wet spells over South America base on observation and the U.S. CLIVAR drought experiments. *J. Clim.* **24**: 1801–1820, doi: 10.1175/JCI3874.1.

Molteni F. 2003. Atmospheric simulations using a GCM with simplified physical parameterizations. I: Model climatology and variability in multi-decadal experiments. *Clim. Dyn.* **20**: 175–191.

Nobre C, Shukla J. 1996. Variations of sea surface temperature, wind stress and rainfall over the tropical Atlantic and South America. *J. Clim.* **9**: 2464–2479.

Podesta G, Letson D, Messina C, Royce F, Ferreyra RA, Jones J, Hansen J, Llovet I, Grondona M, O'Brien JJ. 2002. Use of ENSO-related climate information in agricultural decision making in Argentina: a pilot experience. *Agric. Syst.* **74**(3): 371–392.

Rayner NA, Parker DE, Horton EB, Folland CK, Alexander LV, Rowell DP, Kent EC, Kaplan A. 2003. Global analyses of sea surface temperature, sea ice, and night marine air temperature since the late nineteenth century. *J. Geophys. Res. Atmos.* **108**(D14): 4407, doi: 10.1029/2002JD002670.

Robertson AW, Farrara JD, Mechoso CR. 2003. Simulations of atmospheric response to South Atlantic sea surface temperature anomalies. *J. Clim.* **16**: 2540–2551.

Rodriguez-Fonseca B, Polo I, Garcia-Serrano J, Losada T, Mohino E, Mechoso CR, Kucharski F. 2009. Are Atlantic Niño enhancing Pacific ENSO events in recent decades? *Geophys. Res. Lett.* **36**(20): L20705, doi: 10.1029/2009GL040048.

Saji NH, Goswami BN, Vinayachandra PN, Yamagata T. 1999. A dipole mode in the tropical Indian Ocean. *Nature* **401**: 360–363.

Saji NH, Ambrizzi T, Ferraz SET. 2005. Indian Ocean Dipole mode events and austral surface air temperature anomalies. *Dyn. Atmos. Oceans* **39**: 87–101.

Saravanan R, Chang P. 2000. Interaction between tropical Atlantic variability and El Niño-Southern Oscillation. *J. Clim.* **13**: 2177–2194.

Schneider U, Becker A, Finger P, Meyer-Christoffer A, Rudolf B, Bruno, Ziese M. 2011. GPCC full data reanalysis version 6.0 at 1.0: monthly land-surface precipitation from rain-gauges built on GTS-based and historic data. doi: 10.5676/DWD_GPCC/FD_M_V6_100.

Seager R, Naik N, Baethgen W, Robertson A, Kushnir Y, Nakamura J, Jurburg S. 2010. Tropical oceanic causes of interannual to multidecadal precipitation variability in Southeast South America over the past century. *J. Clim.* **23**: 5517–5539, doi: 10.1175/2010JCLI3578.1.

Silvestri GE. 2004. El Niño signal variability in the precipitation over southeastern South America during the austral summer. *Geophys. Res. Lett.* **31**(18): L18206, doi: 10.1029/2004GL020590.

Smith TM, Reynolds RW, Peterson TC, Lawrimore J. 2008. Improvements to NOAA's historical merged land-ocean surface temperature analysis (1880–2006). *J. Clim.* **21**: 2283–2296.

Tsonis AA, Swanson K, Kravtsov S. 2007. A new dynamical mechanism for major climate shifts. *Geophys. Res. Lett.* **34**(13): L13705, doi: 10.1029/2007GL030288.

Vera C, Silvestri G, Barros V, Carril A. 2004. Differences in El Nino response over the southern hemisphere. *J. Clim.* **17**(9): 1741–1753.

Wang X, Wang C. 2014. Different impacts of various El Niño events on the Indian Ocean dipole. *Clim. Dyn.* **42**: 991–1005.

Wang C, Kucharski F, Barimalala R, Bracco A. 2009. Teleconnections of the tropical Atlantic to the Indian and Pacific Oceans: a review of recent findings. *Meteorol. Z.* **18**: 445–454, doi: 10.1127/0941-2948/2009/0394.

Webster PJ, Moore AM, Loschnigg JP, Leben RP. 1999. Coupled ocean–atmosphere dynamics in the Indian Ocean during 1997–98. *Nature* **401**: 356–360.

Xue Y, Smith TM, Reynolds RW. 2003. Interdecadal changes of 30-yr SST normal during 1871–2000. *J. Clim.* **16**: 1601–1612.

Yoo GH, Kug JS, Park JY, Jin FF. 2013. Sea surface temperature in the north tropical Atlantic as a trigger for El Niño/Southern Oscillation events. *Nat. Geosci.* **6**: 112–116, doi: 10.1038/NGEO1986.

Yoon JH, Zeng N. 2010. An Atlantic influence on Amazon rainfall. *Clim. Dyn.* **34**(2–3): 249–264.

Yulaeva E, Wallace JM. 1994. The signature of the ENSO in global temperature precipitation fields derived from the Microwave Sounding Unit. *J. Clim.* **7**: 1719–1736.

